B_2N Monolayer: a Direct Band-Gap Semiconductor with High and Highly Anisotropic Carrier Mobility

Shuyi Lin[1,#], Yu Guo[2,#], Meiling Xu[1,*], Jijun Zhao[2,†], Yiwei Liang[1], Xuanhao Yuan[1], Yiming Zhang[1], Feilong Wang[1], Jian Hao[1] and Yinwei Li[1,‡]

[1] Laboratory of Quantum Functional Materials Design and Application, School of Physics and Electronic Engineering, Jiangsu Normal University, Xuzhou 221116, China

[2] Key Laboratory of Materials Modification by Laser, Ion and Electron Beams (Dalian University of Technology), Ministry of Education, Dalian 116024, China

Supplementary methods

Carrier mobility calculations

The carrier mobility of two-dimensional materials based on the deformation potential theory was estimated by using the following expression[1–3]:

$$\mu = \frac{e\hbar^3 C_{2D}}{k_B T m^* m_d E_1^2}$$

Here, C_{2D}, E_1 and m^* represent the elastic modulus of the longitudinal strain, the deformation potential constant of the VBM for holes or CBM for electrons, and the carrier effective mass in the transport direction, respectively. The C_{2D} is defined as $C_{2D} = \frac{2(E - E_0)}{S_0\left(\frac{\Delta l}{l_0}\right)^2}$, where E, E_0, S_0, l_0 represent the total energy for the compressed/dilated structure, the total energy at equilibrium, the equilibrium lattice area, the equilibrium lattice constant in the transport direction and the deformation of l_0, respectively. The E_1 equals to $\frac{\Delta E}{(\frac{\Delta l}{l_0})}$, in which E, l, and Δl are donated as the energy change of CBM or VBM under compression or tensile strain, the lattice constants in the transport direction, and the deformation of l_0. m^* is the effective mass in transport direction, and m_d is determined by $m_d = \sqrt{m_x^* m_y^*}$ (m_x^* is perpendicular to m_y^*). The temperature T is set to be 300 K, and k_B is Boltzmann constant.

Absorption spectra calculations

Absorption spectra is expressed by $A(\omega) = 1 - e^{-\alpha(\omega)\cdot\Delta z}$, where $\alpha(\omega) = \frac{\omega\varepsilon_2}{cn}$ is the absorption coefficient, $n = \sqrt{\frac{\varepsilon_1^2 + \varepsilon_2^2 + \varepsilon_1}{2}}$ is the index of refraction, ω is the light frequency, ε_1 and ε_2 are the real and imaginary parts of the dielectric function, *c* is the speed of light in vacuum, Δz represents the unit-cell size in the *c* direction. The electronic structures were obtained from HSE06 level. The *k*-mesh is doubled and the number of bands is twice that of the optimized calculation. To further validate the effectiveness of our calculation, we have calculated the absorption spectra of cd-silicon using the same parameters, and the results is in agreement with the reported ones[4].

Detail on the structure prediction

The particle swarm optimization (PSO) method within the evolutionary algorithm as implemented in the Crystal structure AnaLYsis by Particle Swarm Optimization (CALYPSO) code was employed to find the lowest energy structures of B_xN_y (1 ≤ x, y ≤ 4) monolayers. Unit cells containing 1- 4 formula units (f.u.) were considered. In the first step, random structures with certain symmetry are constructed in which atomic coordinates are generated by the crystallographic symmetry operations. Local optimizations using the VASP code were done with the conjugate gradients method and stopped when Gibbs free energy changes became smaller than 1×10^{-5} eV per cell. After processing the first generation structures, 60% of them with lower Gibbs free energies are selected to construct the next generation structures by PSO. 40% of the structures in the new generation are randomly generated. A structure fingerprinting technique of bond characterization matrix is applied to the generated structures, so that identical structures are strictly forbidden. These procedures significantly enhance the diversity of the structures, which is crucial for structural global search efficiency. In most cases, structural searching simulations for each calculation were stopped after generating 1000~ 1200 structures (e.g., about 20 ~ 30 generations).

Supplementary Tables

Table SI. The calculated elastic constants (C_{ij}, N/m), Young's modulus (E_Y, N/m) and Poisson's ratio (P_r) of B_2N, B_3N and B_4N monolayers.

	C_{11}	C_{22}	C_{12}	C_{66}	E_{Yx}	E_{Yy}	P_{rx}	P_{ry}
B_2N	208.72	161.40	31.62	48.23	202.53	156.61	0.19	0.15

B_3N	157.16	171.14	13.66	90.34	156.07	169.95	0.08	0.09
B_4N	186.85	88.14	29.77	85.47	176.79	83.40	0.34	0.16

Table SII. Carrier mobility and band gap of some 2D materials.

Materials	***x* direction**		***y* direction**		**Band gap (eV)**	**Direct or indirect**	**Refs**
	μ_e	μ_h	μ_e	μ_h			
graphene	339000	322000	320000	351000	0	D	5
graphdiyne	208100	19700	172200	19100	0.46	D	6
phosphorene	1100	640	80	10000	1.51	D	7
Silicene	258000	223000	257000	222000	0	D	8
As	21	66	21	66	2.47	ID	9
Kagome-P	1090	20	1090	1540	1.64	ID	10
Kagome-As	580	40	570	1430	1.9	ID	10
Kagome-Sb	510	120	510	4570	1.71	ID	10
Sb	45	34	15	16	2.38	ID	11
Be_2N_6	10000	1090	9270	1210	1.71	ID	12
h-BN	34	36	34	36	5.6	D	13
BP	49960	13700	68810	26050	0.85	D	9
C_3N	448	155	529	2205	1.22	ID	14
C_2N	41	30	730	332	2.46	D	14
SiS	1400	366	9490	1300	1.22	D	15
Si_3S	15970	8890	106	360	0.94	D	16
Si_3O	12920	7340	136	887	1.19	D	16
SiAs	1250	390	310	1120	2.37	D	17
PC_6	294000	248000	3160	164000	0.84	D	18
P_3Cl_2	740	700	56890	26450	2.41	D	19
CaP_3	10000	80	1000	780	1.15	D	20
ScN	117000	14	12200	137	1.39	D	21
GaSe	73	1181	58	70	2.94	ID	22
GaTe	992	128044	600	547	1.88	ID	22
GeS	2430	116	320	60	2.29	ID	23
GeSe	4032	323	1555	76	1.59	D	23
GeAs	2380	280	1170	550	2.04	D	17
GeTe	1049	294	603	1066	2.35	D	24
As_2S_3	253	10	168	13	3.11	ID	25
MoS_2	72	184	73	212	1.81	D	26
BCN	176	88	23	164	3.19	ID	27
BC_2N	52550	14820	3700	270	1.6	D	28
BCP	1590	1610	2290	840	1.18	D	27
PC_6N	36	13700	30	10	2.56	ID	29
Ti_2CO_2	611	74100	254	22500	1.28	D	30
Zr_2CO_2	83	2300	1096	1695	1.76	D	30
Hf_2CO_2	126	2192	2270	1598	1.79	D	30
TiNF	500	2100	550	1000	1.52	D	31

TiNCl	550	1900	1100	2500	1.42	D	[31]
TiNBr	800	1800	1700	2500	1.40	D	[31]
$CrPbTe_3$	62	129	31	79	0.25	ID	[32]
CuLiSe	3019	266	3019	266	1.60	D	[33]
CuLiTe	2766	494	2766	494	1.85	D	[33]
$Zn_2C_2P_2$	145	98689	10024	2361	1.16	D	[34]
MoSSe	530	58	490	55	2.02	D	[35]
PdPS	312	13	55	249	2.12	I	[36]
PdPSe	197	0.34	2.04	344.33	1.95	I	[36]

Table SIII. The optimized structural parameters of B_2N, B_3N, and B_4N monolayers.

Space group	Compound	a, b, c (Å) α, β, γ (deg)	Atomic position
$P1$	B_4N_3	$a=6.8226$ $b=6.8228$ $c=25.1132$ $\alpha=92.771$ $\beta=94.2301$ $\gamma=60.0012$	B1(1a) (0, 0, 0.50057) B2(1a) (0.33334,0.33335,0.50060) B3(1a) (0.62705, 0.47124,0.50058) B4(1a) (0.90168, 0.62706, 0.50053) B5(1a) (0.47122, 0.90175, 0.50056) B6(1a) (0.05291, 0.20754, 0.50058) B7(1a) (0.73957, 0.05286, 0.50057) B8(1a) (0.20755, 0.73955, 0.50057) N1(1a) (0.14486,0.56511, 0.50055) N2(1a) (0.29002, 0.14489, 0.50061) N3(1a) (0.56513, 0.29001, 0.50062) N4(1a) (0.70238, 0.86015, 0.50052) N5(1a) (0.43747, 0.70240, 0.50059) N6(1a) (0.86016, 0.43743, 0.50054)
$P4/mbm$	B_3N_2	$a=b=7.8011$ $c=34.7066$ $\alpha=\beta=\gamma=90$	B1(4h) (0.92162, 0.57838, 0.5) B2(8j) (0.79886, 0.85661, 0.5) N(8j) (0.03779, 0.23684, 0.5)
$Amm2$	B_2N	$a=10.3074$ $b=3.9085$ $c=29.6758$ $\alpha=\beta=\gamma=90$	B1(4*e*) (0.18329, 0.17110,0.5) B2(4*e*) (0.91652, 0.81329,0.5) N(4*e*) (0.17950, 0.54204,0.5)
Cm	B_3N	$a=17.1327$ $b=2.6239$ $c=31.8362$ $\alpha=\gamma=90$ $\beta=92.0106$	B1(2*a*) (0.04209, 0.5, 0.49559) B2(2*a*) (0.29435, 0.5, 0.50877) B3(2*a*) (0.38528, 0.5, 0.48601) B4(2*a*) (0.16873, 0, 0.50239) B5(2*a*) (0.44426, 0, 0.48942) B6(2*a*) (0.35416, 0, 0.50881) N1(2*a*) (0.21026, 0.5, 0.50455) N2(2*a*) (0.08415, 0, 0.49779)
$C2/m$	B_4N	$a=10.37839$	B1(4*i*) (0.45919, -0.5, 0.50157)

	b=2.6918	B2(4i) (0.68824, -0.5, 0.49117)
	c=60.8509	B3(4i) (0.64321, -1, 0.49385)
	α=γ=90	B4(4i) (0.27345, 0, 0.49812)
	β=100.7124	N(4i) (0.42552, 0, 0.50286)

Table SIV. The energy differences between AA and AB stacking calculated by nonlocal optB86b-vdW density functional, optB88-vdw density functional and DFT-D2 method.

Energy	Methods			
(eV/atom)	optB86b	optB88	DFT-D2	PBE
E_{AA}	0.02117	0.01528	0.02539	-0.001
E_{AB}	0	0	0	0

Supplementary Figures

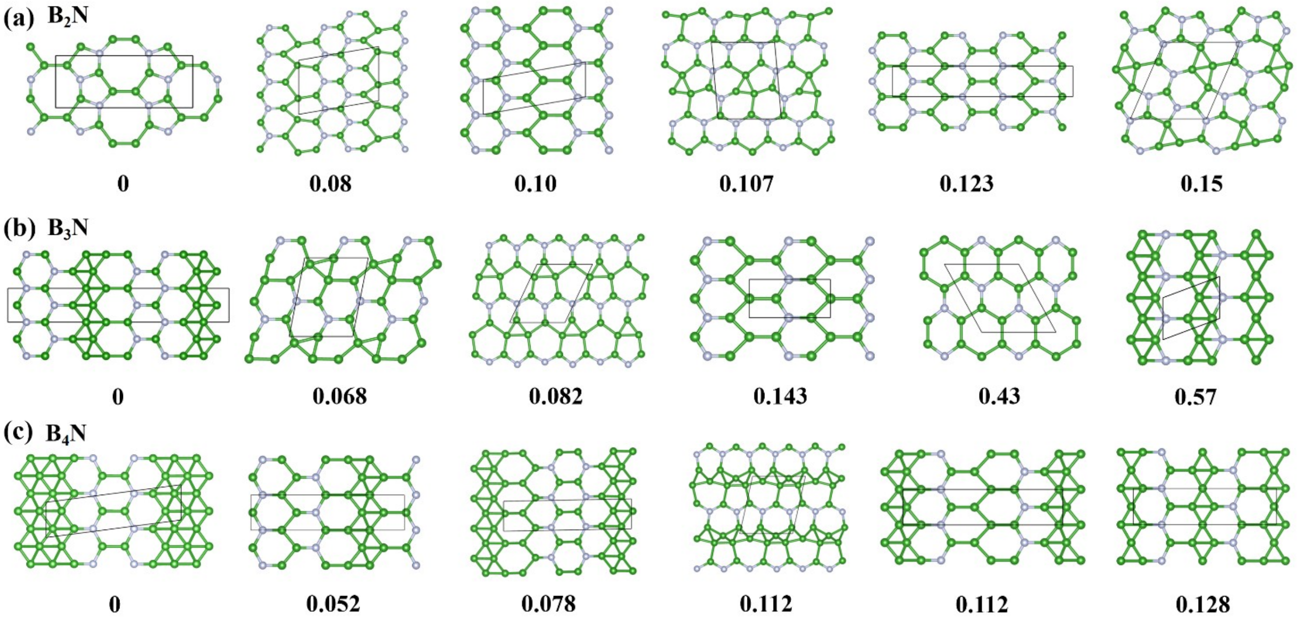

Figure S1. Low-energy structures and the energy differences (eV/atom) relative to ground state structures.

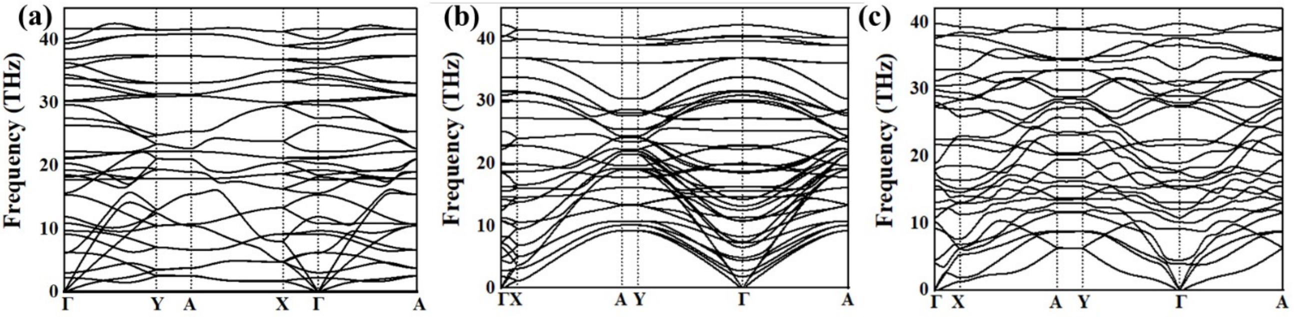

Figure S2. Phonon dispersion curves of (a) B_2N, (b) B_3N and (c) B_4N monolayers

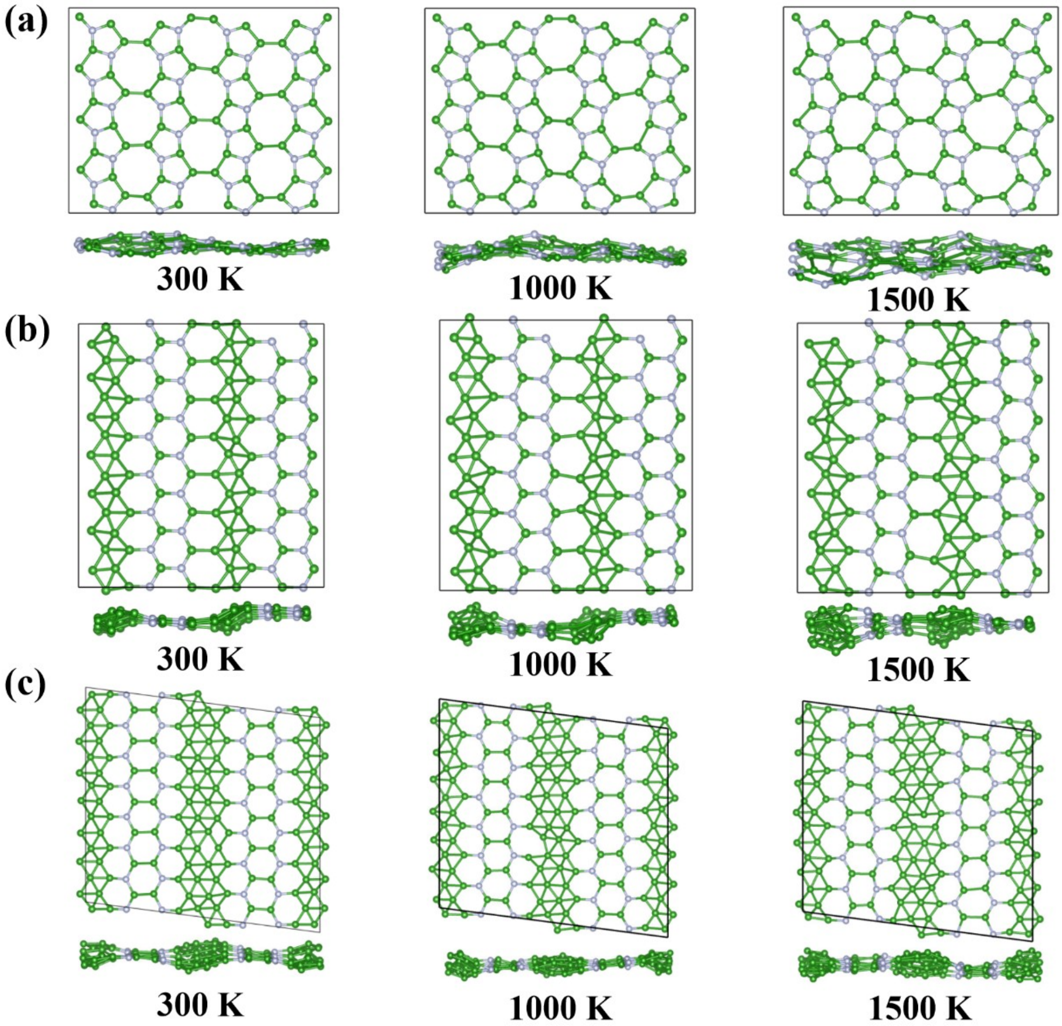

Figure S3. Snapshots of the final frame of each molecular dynamic simulation at 300, 1000 and 1500 K for (a) B_2N, (b) B_3N and (c) B_4N after 6 ps of simulated annealing.

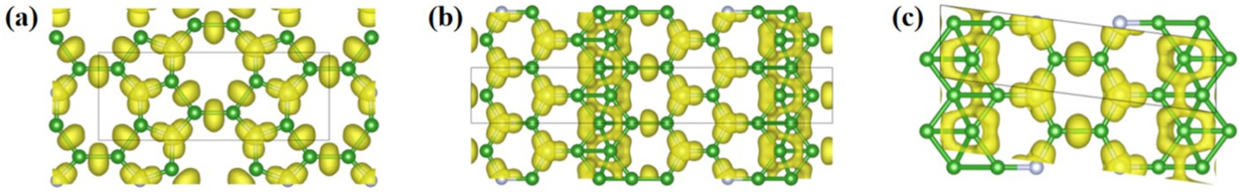

Figure S4. Three-dimensional electron localization functions (isosurface value = 0.75) of (a) B_2N, (b) B_3N and (c) B_4N.

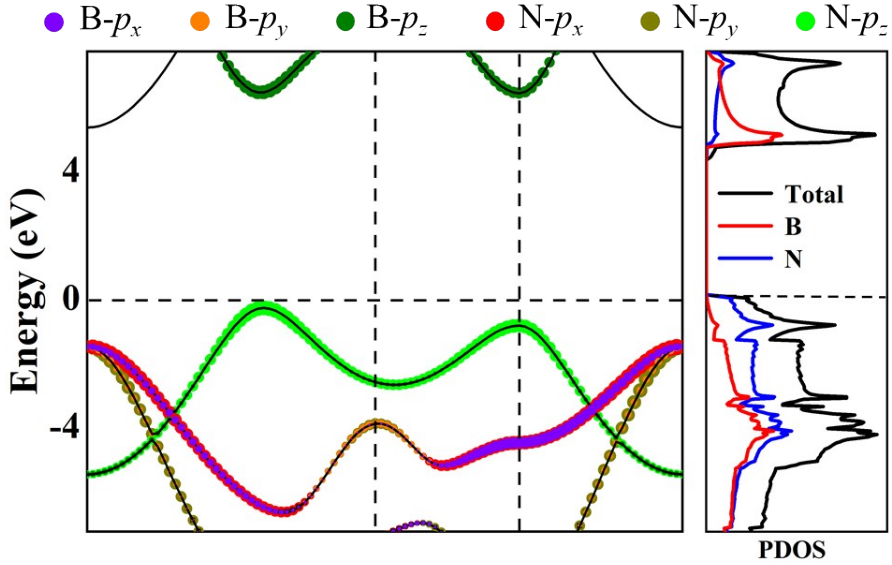

Figure S5. Orbit-resolved band structures and PDOS for *h*-BN.

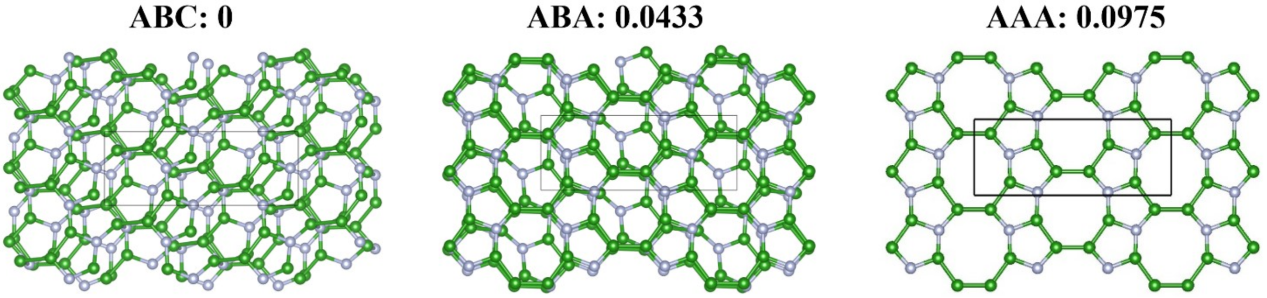
ABC: 0

ABA: 0.0433

AAA: 0.0975

Figure S6. The three stacking configurations of trilayer B_2N and the energy differences (eV/atom) relative to ABC stacking using the optB68b-vdW functional.

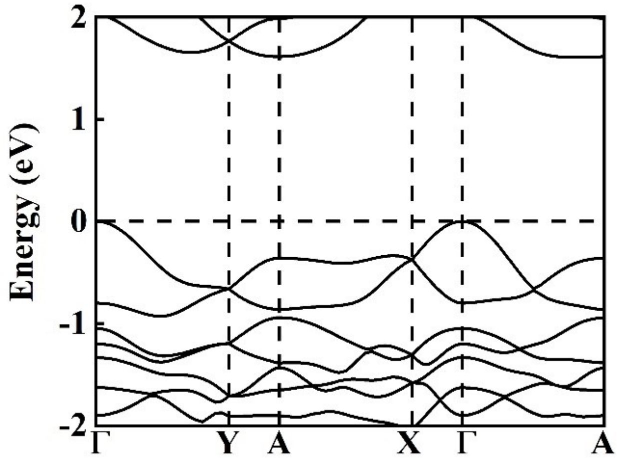

Figure S7. The band structure of ABC stacking of B_2N at the HSE06 level.

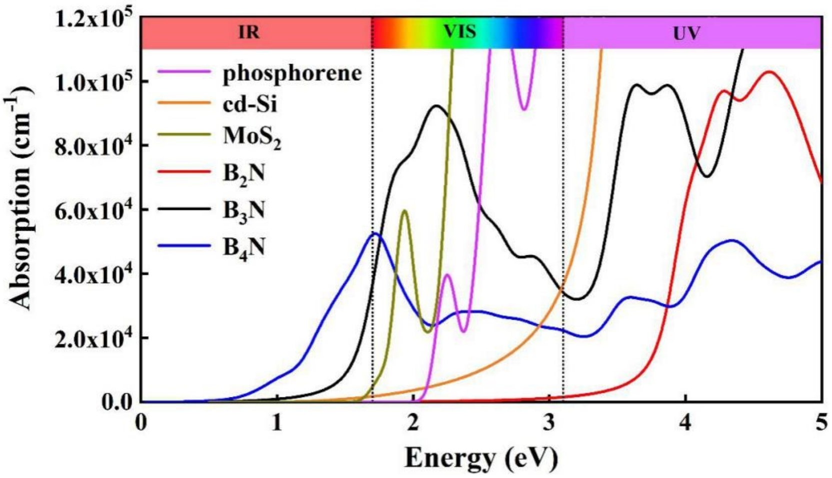

Figure S8. Adsorption spectra of B_2N, B_3N and B_4N monolayers compared to that of phosphorene, diamond silicon (cd-Si) and MoS_2 monolayer.

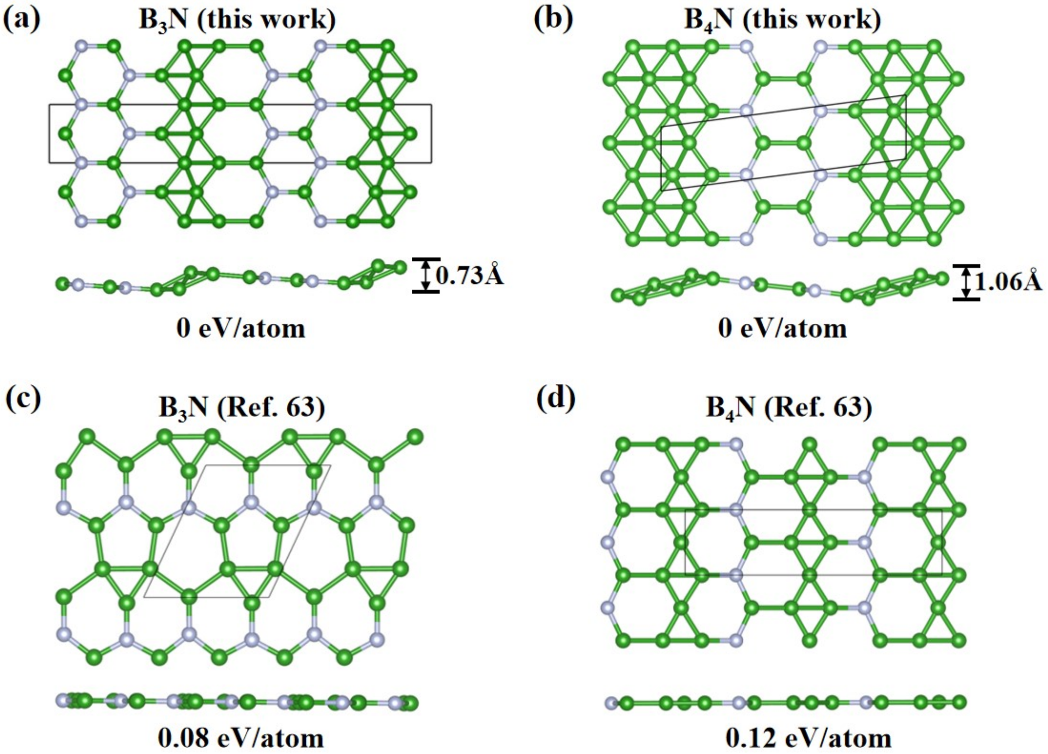

Figure S9. The crystal structures of predicted B_3N and B_4N monolayers and their energy differences.

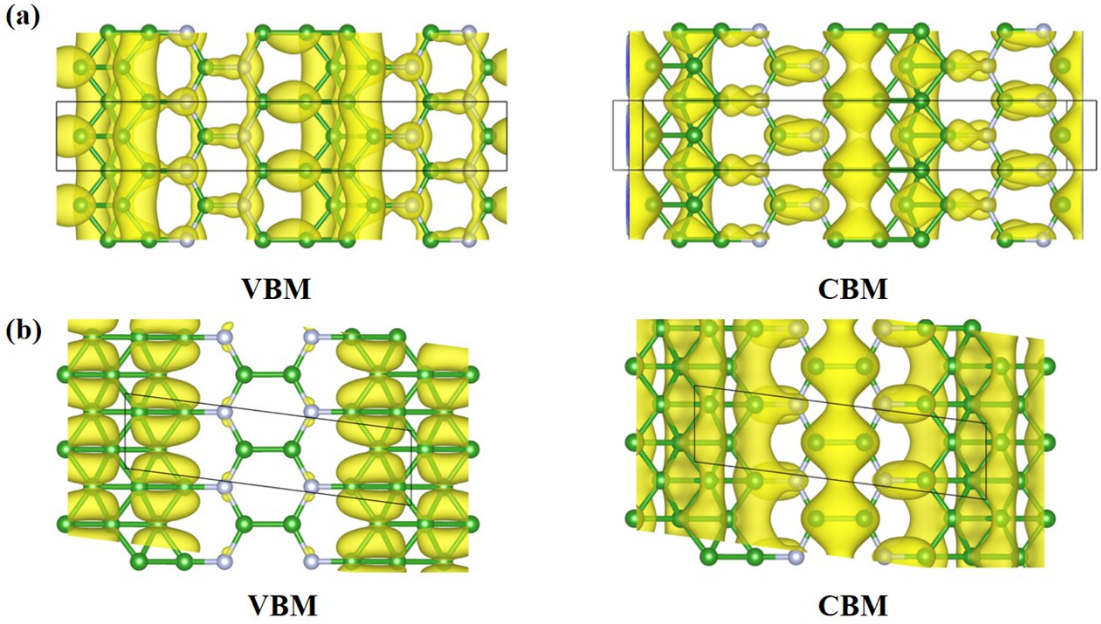

Figure S10. Partial charge density of the VBM and the CBM for B_3N (a-b) and B_4N (c-d), respectively. Band decomposed charge densities calculations suggest that both VBM and CBM of B_3N are mainly attributed by the π bonds from hybridized B-B *p* orbital electrons, while VBM and CBM of B_4N are contributed by the σ bonds and π bonds from hybridized B-B *p* orbital electrons, respectively.

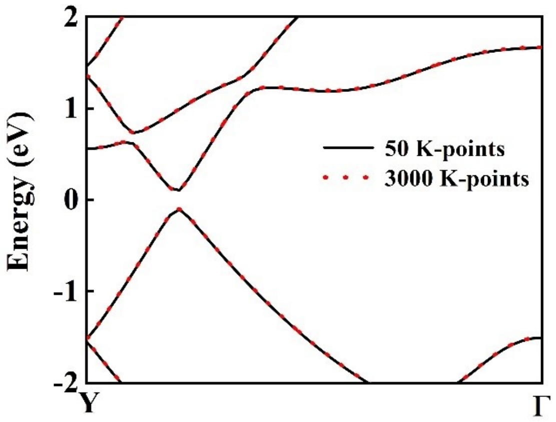

Figure S11. The band structure of B_4N monolayer along the Y→ Γ direction using (a) 50 K-points and (b) 3000 K-points at the PEB level.

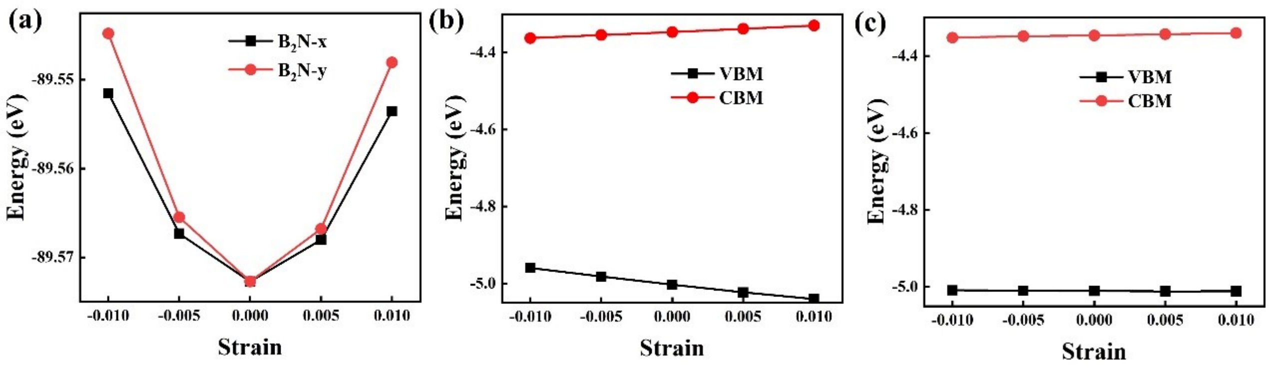

Figure S12. (a) The total energy difference of B_2N monolayer at the strain between -1% to 1% along the *x* and *y* directions. Energy shift of CBM and VBM for B_2N with respect to the vacuum energy as a function of lattice dilation and compression along the (b) x and (c) y directions.

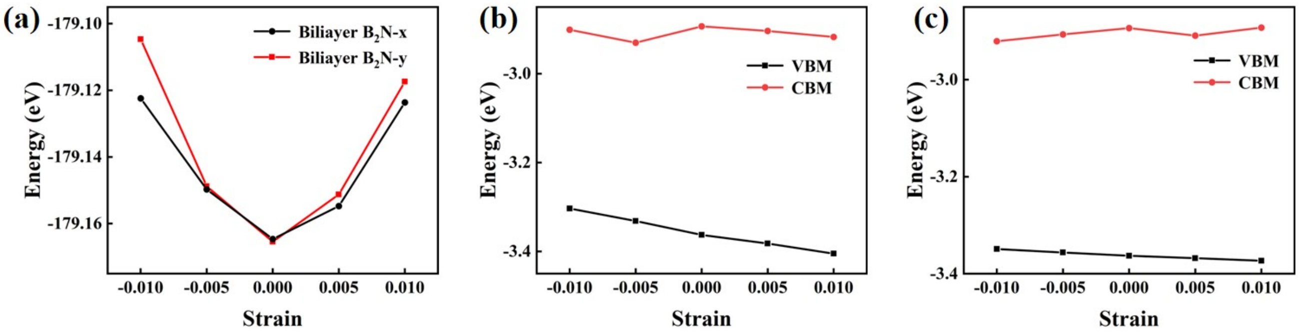

Figure S13. (a) The total energy difference of AB stacking of B_2N at the strain between -1% to 1% along the x and y directions. Energy shift of CBM and VBM for bilayer B_2N with respect to the vacuum energy as a function of lattice dilation and compression along the (b) x and (c) y directions.

Supplementary References

[1] G. Fiori and G. Iannaccone, Multiscale Modeling for Graphene-Based Nanoscale Transistors, *Proc. IEEE*, 2013, **101**, 1653–1669.

[2] S. Takagi, A. Toriumi, M. Iwase and H. Tango, On the universality of inversion layer mobility in Si MOSFET's: Part I-effects of substrate impurity concentration, *IEEE Trans. Electron Devices*, 1994, **41**, 2357–2362.

[3] S. Bruzzone and G. Fiori, Ab-initio simulations of deformation potentials and electron mobility in chemically modified graphene and two-dimensional hexagonal boron-nitride, *Appl. Phys. Lett.*, 2011, **99**, 222108.

[4] J. H. Yang, Y. Zhai, H. Liu, H. Xiang, X. Gong and S. H. Wei, Si_3AlP: A new promising material for solar cell absorber, *J. Am. Chem. Soc.*, 2012, **134**, 12653–12657.

[5] E. H. Hwang and S. Das Sarma, Acoustic phonon scattering limited carrier mobility in two-dimensional extrinsic graphene, *Phys. Rev. B*, 2008, **77**, 115449.

[6] M. Long, L. Tang, D. Wang, Y. Li and Z. Shuai, Electronic Structure and Carrier Mobility in Graphdiyne Sheet and Nanoribbons: Theoretical Predictions, *ACS Nano*, 2011, **5**, 2593–2600.

[7] J. Qiao, X. Kong, Z.-X. Hu, F. Yang and W. Ji, High-mobility transport anisotropy and linear dichroism in few-layer black phosphorus, *Nat. Commun.*, 2014, **5**, 4475.

[8] Z.-G. Shao, X.-S. Ye, L. Yang and C.-L. Wang, First-principles calculation of intrinsic carrier mobility of silicene, *J. Appl. Phys.*, 2013, **114**, 93712.

[9] Y. Wang, P. Huang, M. Ye, R. Quhe, Y. Pan, H. Zhang, H. Zhong, J. Shi and J. Lu, Many-body Effect, Carrier Mobility, and Device Performance of Hexagonal Arsenene and Antimonene, *Chem. Mater.*, 2017, **29**, 2191–2201.

[10] J. Zhu, C. He, Y. Zhao and B. Fu, Kagome-like group-VA monolayers with indirect–direct band gap transition and anisotropic mobility, *J. Mater. Chem. C*, 2020, **8**, 2732–2740.

[11] S. H. Mir, Exploring the electronic, charge transport and lattice dynamic properties of two-dimensional phosphorene, *Phys. B Condens. Matter*, 2019, **572**, 88–93.

[12] F. Li, Y. Wang, H. Wu, Z. Liu, U. Aeberhard and Y. Li, Benzene-like N_6 rings in a Be_2N_6 monolayer: a stable 2D semiconductor with high carrier mobility, *J. Mater. Chem. C*, 2017, **5**, 11515–11521.

[13] S. Grenadier, A. Maity, J. Li, J. Y. Lin and H. X. Jiang, Lateral charge carrier transport properties of B-10 enriched hexagonal BN thick epilayers, *Appl. Phys. Lett.*, 2019, **115**, 72108.

[14] S. Bu, N. Yao, M. A. Hunter, D. J. Searles and Q. Yuan, Design of two-dimensional carbon-nitride structures by tuning the nitrogen concentration, *npj Comput. Mater.*, 2020, **6**, 128.

[15] J.-H. Yang, Y. Zhang, W.-J. Yin, X. G. Gong, B. I. Yakobson and S.-H. Wei, Two-Dimensional SiS Layers with Promising Electronic and Optoelectronic Properties: Theoretical Prediction, *Nano Lett.*, 2016, **16**, 1110–1117.

[16] A. Jalil, S. Zafar, S. Ahmed, A. Hassan and D. Li, Surface Science A new 2D Si_3X (X = S , O) direct band gap semiconductor with anisotropic carrier mobility, *Surf. Sci.*, 2021, **704**, 121736.

[17] P. Li, W. Wu, Y. Xu, J. Liu, S. Wu, Y. Ye, C. Liang and X. C. Zeng, Two-Dimensional IV–V Monolayers with Highly Anisotropic Carrier Mobility and Electric Transport Properties, *J. Phys. Chem. Lett.*, 2021, **12**, 1058–1065.

[18] T. Yu, Z. Zhao, Y. Sun, A. Bergara, J. Lin, S. Zhang, H. Xu, L. Zhang, G. Yang and Y. Liu, Two-Dimensional PC 6 with Direct Band Gap and Anisotropic Carrier Mobility, *J. Am. Chem. Soc.*, 2019, **141**, 1599–1605.

[19] N. Lu, Z. Zhuo, Y. Wang, H. Guo, W. Fa, X. Wu and X. C. Zeng, P_3Cl_2: A Unique Post-Phosphorene 2D Material with Superior Properties against Oxidation., *J. Phys. Chem. Lett.*, 2018, **9**, 6568–6575.

[20] N. Lu, Z. Zhuo, H. Guo, P. Wu, W. Fa, X. Wu and X. C. Zeng, CaP_3: A New Two-Dimensional Functional Material with Desirable Band Gap and Ultrahigh Carrier Mobility., *J. Phys. Chem. Lett.*, 2018, **9**, 1728–1733.

[21] D. Liang, T. Jing, M. Deng and S. Cai, Two-dimensional ScN with high carrier mobility and unexpected mechanical properties, *Nanotechnology*, 2021, **32**, 155201.

[22] B. Marfoua and J. Hong, High thermoelectric performance in two dimensional chalcogenides systems: GaSe and GaTe, *Nanotechnology*, 2021, **32**, 115702.

[23] X. Lv, W. Wei, Q. Sun, F. Li, B. Huang and Y. Dai, Two-dimensional germanium monochalcogenides for photocatalytic water splitting with high carrier mobility, *Appl. Catal. B Environ.*, 2017, **217**, 275–284.

[24] M. Qiao, Y. Chen, Y. Wang and Y. Li, The germanium telluride monolayer: a two dimensional semiconductor with high carrier mobility for photocatalytic water splitting, *J. Mater. Chem. A*, 2018, **6**, 4119–4125.

[25] X. Liu, Z. Zhang, Z. Ding, B. Lv, Z. Luo, J. Wang and Z. Gao, Highly anisotropic electronic and mechanical properties of monolayer and bilayer As_2S_3, *Appl. Surf. Sci.*, 2021, **542**, 148665.

[26] A. Rawat, N. Jena, D. Dimple and A. De Sarkar, A comprehensive study on carrier mobility and artificial photosynthetic properties in group VIB transition metal dichalcogenide monolayers, *J. Mater. Chem. A*, 2018, **6**, 8693–8704.

[27] V. K. Yadav, S. H. Mir and J. K. Singh, A computational study of structural, electronic and carrier mobility of boron and phosphorus/nitrogen co-doped graphene, *Phys. B Condens. Matter*, 2019, **571**, 291–295.

[28] M. S. Si, J. Xie, Z. Y. Zhang, D. Z. Yang and D. S. Xue, Theoretical prediction of carrier mobility in few-layer BC_2N, *J. Phys. Chem. Lett.*, 2014, **5**, 4073–4077.

[29] C. Wang, T. Yu, A. Bergara, X. Du, F. Li and G. Yang, Anisotropic PC_6N Monolayer with Wide Band Gap and Ultrahigh Carrier Mobility, *J. Phys. Chem. C*, 2020, **124**, 4330–4337.

[30] Z. Guo, J. Zhou, L. Zhu and Z. Sun, MXene: a promising photocatalyst for water splitting, *J. Mater. Chem. A*, 2016, **4**, 11446–11452.

[31] C. Wang and G. Gao, Titanium nitride halides monolayers: promising 2D anisotropic thermoelectric materials, *J. Phys. Condens. Matter*, 2020, **32**, 205503.

[32] B. Marfoua and J. Hong, Spin Seebeck effect in the 2D ferromagnetic $CrPbTe_3$, *Phys. E Low-dimensional Syst. Nanostructures*, 2021, **126**, 114443.

[33] K. Jia, C.-L. Yang, M.-S. Wang, X.-G. Ma and Y.-G. Yi, First-principles investigation on the thermoelectric performance of half-Heusler compound CuLiX(X = Se, Te), *J. Phys. Condens. Matter*, 2021, **33**, 95501.

[34] X. Liu, X. Shao, Y. Zheng, S. Qi, M. Zhang, H. Li, C. Li, M. Tan, D. Zheng and M. Zhao, Prediction of a ternary two-dimensional pentagonal $Zn_2C_2P_2$ monolayer for photocatalytic water splitting with high carriers mobility, *Appl. Surf. Sci.*, 2020, **518**, 146197.

[35] X. Ma, X. Wu, H. Wang and Y. Wang, A Janus MoSSe monolayer: a potential wide solar-spectrum water-

splitting photocatalyst with a low carrier recombination rate, *J. Mater. Chem. A*, 2018, **6**, 2295–2301.

[36] Y. Jing, Y. Ma, Y. Wang, Y. Li and T. Heine, Ultrathin Layers of PdPX (X=S, Se): Two Dimensional Semiconductors for Photocatalytic Water Splitting, *Chem. - A Eur. J.*, 2017, **23**, 13612–13616.